

Capillary Device Passive Thermal Conditioning

M. H. Blatt*

General Dynamics Convair Division, San Diego, Calif.

and

J. C. Aydelott†

NASA Lewis Research Center, Cleveland, Ohio

An upgraded Centaur capability was studied by investigating deployment of capillary devices for propellant acquisition. Analytical and experimental investigation of promising capillary pumping concepts for passive cooling of cryogenic capillary acquisition devices resulted in selection, test, and empirical correlation of four wicking configurations. Only plate/screen-screen/plate and plate/screen-plate/screen configurations would function successfully under worst-case Centaur D-1S conditions. Weight estimates were developed for the passively cooled configurations and comparisons were made of passive and actively cooled capillary devices.

Nomenclature

A_F	= cross-sectional area of the wicking front
C	= constant depending upon cross-sectional shape
D_H	= hydraulic diameter of wicking cross section
f	= Fanning friction factor = $1/4$ Blasius friction factor
F	= surface force
g	= ambient acceleration level
g_c	= a dimensional constant
K	= constant determined analytically for each configuration
L	= distance from liquid pool to wicking front
\dot{m}	= wicking mass flow rate
ΔP_f	= frictional pressure loss = $KL^2/\Delta t$
ΔP_x	= correction term
ΔP_σ	= surface tension driving pressure
\dot{Q}	= $\dot{m}\lambda$
R_1, R_2	= principle radii of curvature of the liquid wicking front
R_E	= effective capillary radius = $2A_F/(\text{WP-width})$
Re	= Reynolds number = $(\rho V D_H)/\mu$
Δt	= time from initiation of wicking
V	= liquid wicking velocity
w	= width of a single capillary
W	= width of the capillary device surface
WP	= wetted perimeter of the wicking front
θ	= angle of wicking direction with horizontal
λ	= heat of vaporization
μ	= liquid viscosity
ρ	= fluid density
σ	= liquid surface tension
ϕ	= contact angle, zero for LH_2 and LO_2

Introduction

THE use of capillary devices for replacing the baseline hydrogen peroxide settling system on Centaur is discussed in detail in Ref. 1. Preliminary analysis and weight comparisons indicated that passively cooled start baskets, fabricated from fine-mesh screen materials, together with thermal subcoolers (for replacing the main tank

Presented as Paper 77-851 at the AIAA/SAE 13th Propulsion Conference, Orlando, Fla., July 11-13, 1977; submitted July 11, 1977; revision received Feb. 10, 1978. Copyright © American Institute of Aeronautics and Astronautics, Inc., 1977. All rights reserved.

Index categories: Thermal Control; LV/M Propulsion and Propellant Systems.

*Senior Thermodynamics Engineer. Member AIAA.

†Aerospace Engineer.

pressurization system) were promising for multiple-burn missions. Passive capillary acquisition thermal conditioning offers reduced complexity, hardware weight, and vented fluid weight compared to an actively cooled system for preventing screen dryout (maintaining wet screens) between burns. Work performed in the study analytically and experimentally examined wicking configurations that could enhance the heat interception capability of a screen alone.

The baseline vehicle configuration was the Centaur D-1S.² The Centaur D-1S, as defined during the foregoing contract, represented a minimum-change D-1T configuration (Centaur currently used with Titan), modified to be compatible with the Space Shuttle interface, operations, and safety requirements. Approximately 95% of the existing Centaur components remain unchanged for the D-1S. Figure 1 summarizes significant modifications made to the existing D-1T to evolve the D-1S configuration.

Passive Thermal Conditioning

Wicking configurations for passive thermal conditioning were evaluated by establishing the ground rules of the study, determining the method of analysis, and selecting the most promising configurations for satisfying heat flux interception requirements. Fabricability of each wick configuration was assessed for LO_2 and LH_2 Centaur D-1S start basket cooling requirements. Wick configurations were selected for testing, and test results obtained with ethanol were compared to analytical predictions of wicking versus time.

Heat-transfer conditions that could cause screen drying were examined for all start basket screened surfaces for

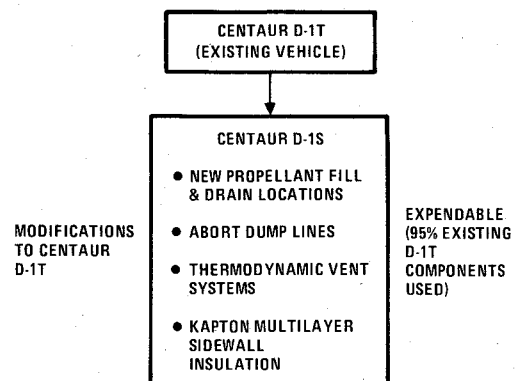


Fig. 1 Evolution of the existing Centaur D-1T to a Centaur compatible with Space Shuttle.

Centaur D-1S mission conditions. Local heat-transfer coefficients as well as average heat-transfer coefficients were established for forced convection, free convection, and conduction with vapor adjacent to the start basket screened surfaces. Total fluid vaporized, assuming interception of heat by wicking, was determined for each portion of the mission for both the oxygen and hydrogen capillary device. Only mission conditions were considered where there was a possibility that the entire basket could be surrounded by vapor. Vapor volumes generated were translated into wicking distances for each basket surface, assuming worst-case vapor location in the start baskets.

Worst-case wicking distance, heat flux, and acceleration conditions were determined for all stages of the missions. This distance varied from 0.31 to 2.41 ft. The range of heat fluxes incident on the capillary device was 0.3 to 11.2 Btu/h-ft². Acceleration levels of interest ranged from 9×10^{-4} to 8.5×10^{-3} g. A detailed matrix of worst-case wicking rate requirements is presented in Ref. 3.

Analysis

The pressure differentials of interest are those dependent upon surface tension ΔP_σ , gravity ΔP_g , and viscosity ΔP_f (laminar frictional pressure loss). Momentum losses can normally be neglected for the low flow rates that occur during wicking. The pressure differentials are related by

$$\Delta P_\sigma = \Delta P_g + \Delta P_f \quad (1)$$

Expressions were derived for the surface tension pressure differential

$$\Delta P_\sigma = \sigma(1/R_1 + 1/R_2) \approx F/A_F \quad (2)$$

The surface force $F = \sigma$ (WP), where WP is the wetted perimeter of the wicking front.

Surface tension pressure differentials were derived for each configuration of interest (Table 1), using Eq. (2). For open channels, the results of Bressler and Wyatt⁴ were also used to compute the surface tension pressure. They found that an expression

$$\Delta P_\sigma = 2\sigma \cos\phi/R_E$$

successfully correlated their data. The frictional pressure drop was computed using

$$\Delta P_f = \frac{2fL\rho V^2}{D_H g_c}$$

The friction factor is normally expressed as a function of Reynolds number

$$f = C/Re$$

Thus,

$$\Delta P_f = \frac{2C\dot{m}\mu L}{D_h^2 A_F g_c} \quad (3)$$

The hydrostatic pressure differential is

$$\Delta P_g = \rho g_c L \sin\theta \quad (4)$$

Equations (1) and (3) were combined and manipulated to yield the heat rate interception capability of a wicking barrier for a single capillary.

$$\dot{Q} = \frac{\rho \lambda g_c D_h^2 A_F}{2C\mu L} [\Delta P_\sigma - \Delta P_g] \quad (5)$$

For thermal conditioning purposes, it is clearer to express the wicking capability in terms of heat rate per unit width, \dot{Q}/W . For a heat source acting alone a line at distance L from the liquid pool this is

$$\frac{\dot{Q}}{W} = \frac{\rho \lambda g_c D_h^2 A_F}{2C\mu L w} [\Delta P_\sigma - \Delta P_g] \quad (6)$$

Equation (5), the heat rate interception capability for a single capillary, is transformed into Eq. (6), the heat rate interception capability for a capillary device surface by multiplying Eq. (5) by the number of capillaries (W/w) in that surface.

For a distributed heat source, $\dot{Q}/A = \dot{Q}/(WL)$, which is equivalent to evaluating Eq. (6) for \dot{Q}/W at a distance L from the liquid pool. All heat interception can thus be expressed in terms of \dot{Q}/W . Equations for computing the \dot{Q}/W capability of each candidate wicking configuration are given in Table 1 with Eqs. (2) and (4) substituted into Eq. (6).

Heat flux interception capability determined from the equations given in Table 1 was compared to the wicking rate requirements. This evaluation produced optimum, minimum, and maximum spacings or wick dimensions that could intercept all heat flux conditions for each wick for both LO₂ and LH₂. Details of this procedure are discussed thoroughly in Ref. 3.

The manufacturing feasibility of each of these configurations was assessed. Flow optimization of the triangular and equilateral triangular wick geometry was restricted to square and equilateral triangle dimensions since they would be easiest to manufacture. The screens and parallel plates are the most isotropic in terms of capillary pumping capability. Other configurations show a decided directional preference and would require two orthogonal layers of wick to satisfy all heat flux interception conditions.

Based on the manufacturing feasibility assessment, four configurations were selected for experimental evaluation. Fine-mesh screen spotwelded to perforated plate was used to create wicking configurations that were selected for their ease of fabrication. These configurations were: plate/screen-screen/plate, plate/screen-plate/screen, and screen/plate-plate/screen. Pleated screen was selected because it offers design flexibility in permitting increased screen area (and thus low pressure drop transverse to the capillary barrier) as the ratio of screen flow area to projected area is increased. Optimum wicking configurations were determined for ethanol wicking in normal gravity, using the equations given in Table 1 for three specimen angles. As discussed in Ref. 3, the upper limit on spacing was controlled by wicking height and the lower limit was controlled by minimum manufacturing tolerances. Wick geometries selected are summarized in Table 2. Perforated plate used was 0.0225-in. thick with 3/8-in. holes on 0.50-in. centers (51% open area).

Test specimens were 3-in. wide and 18-in. long. With the exception of one wicking configuration employing 200 × 1400 mesh, all screens used were 50 × 250 mesh.

Wicking Apparatus

Test specimens were mounted on an aluminum baseplate, which was enclosed in a transparent box, as shown in Fig. 2. A glass plate was used for the top cover of the box for viewing and photographically recording data. Glass was used because it is clearer than plastic and less susceptible to scratching or crazing. The sides of the enclosure, the fluid reservoir, reservoir refill, and leveling devices were Lexan polycarbonate. This material was chosen over glass because of its machinability. Joints were cemented leak-tight and reinforced with screws as required. The transparent glass cover was not cemented to the test enclosure. The cover could thus be removed without disturbing the test specimens, baseplate, or test enclosure. Baseplate orientation was controlled by adjusting three pointed screws.

Table 1 Candidate wicking configurations


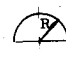
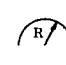
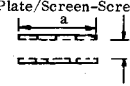
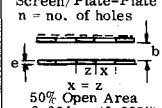
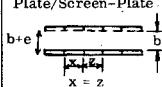
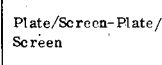
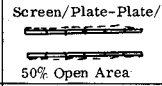

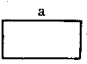
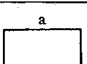
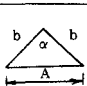
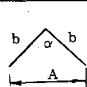
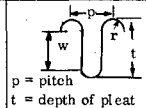
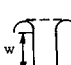
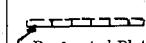
Config.	Sketch	ΔP_f	ΔP_σ	\dot{Q}_T/W
Circle		$\frac{8 \dot{m} \mu L}{\rho \pi R^4 g_c}$	$\frac{2 \sigma}{R}$	$\frac{\rho \lambda \pi R^3 g_c}{8 \mu L} \left[\frac{2 \sigma}{R} - \frac{\rho g_c}{g_c} L \sin \theta \right]$
Closed Semicircle		$\frac{16 \dot{m} \mu L (\pi + 2)}{\rho \pi^3 R^4 g_c}$	$\frac{2 (\pi + 2) \sigma}{\pi R}$	$\frac{\rho \lambda R^3 g_c \pi^3}{32 \mu L (\pi + 2)^2} \left[\frac{2 (\pi + 2) \sigma}{\pi R} - \frac{\rho g_c}{g_c} L \sin \theta \right]$
Open Semicircle		$\frac{16 \dot{m} \mu L}{\rho \pi R^4 g_c}$	$\frac{2 \sigma}{R}$	$\frac{\rho \lambda R^3 g_c \pi}{32 \mu L} \left[\frac{2 \sigma}{R} - \frac{\rho g_c}{g_c} L \sin \theta \right]$ $\frac{\rho \lambda R^3 \pi g_c}{32 \mu L} \left[\frac{2 (\pi - 2) \sigma}{\pi R} - \frac{\rho g_c}{g_c} L \sin \theta \right]$
Parallel Plates		$\frac{12 \dot{m} \mu L}{\rho a^3 b g_c}$	$\frac{2 \sigma}{b}$	$\frac{\rho \lambda b^3 g_c}{12 \mu L} \left[\frac{2 \sigma}{b} - \frac{\rho g_c}{g_c} L \sin \theta \right]$
Parallel Plates		$\frac{3 \dot{m} \mu L (3a + 8ne)^2}{4 \rho (b + e)^3 a^3 g_c}$	$\frac{(3a + 8ne) \sigma}{2(b + e)a}$	$\frac{4 \rho \lambda (b + e)^3 a^2 g_c}{3 \mu L (3a + 8ne)^2} \left[\frac{\sigma (3a + 8ne)}{2(b + e)a} - \frac{\rho g_c}{g_c} L \sin \theta \right]$
Parallel Plates		$\frac{6 \dot{m} \mu L (3a + 4ne)^2}{\rho (2b + e)^3 a^3 g_c}$	$\frac{(3a + 4ne) \sigma}{(2b + e)a}$	$\frac{\rho \lambda (2b + e)^3 a^2 g_c}{6 \mu L (3a + 4ne)^2} \left[\frac{(3a + 4ne) \sigma}{(2b + e)a} - \frac{\rho g_c}{g_c} L \sin \theta \right]$
Parallel Plates		$\frac{96 \dot{m} \mu L (a + ne)^2}{\rho a^3 (2b + e)^3 g_c}$	$\frac{4(a + ne) \sigma}{a(2b + e)}$	$\frac{\rho \lambda (2b + e)^3 a^2 g_c}{96 \mu L (a + ne)^2} \left[\frac{2 \sigma (2a + 2ne)}{a(2b + e)} - \frac{\rho g_c}{g_c} L \sin \theta \right]$
Parallel Plates		$\frac{12 (a + 2ne)^2 \dot{m} \mu L}{(b + e)^3 a^3 \rho g_c}$	$\frac{2(a + 2ne) \sigma}{(b + e)a}$	$\frac{\rho \lambda g_c (b + e)^3 a^2}{12 \mu L (a + 2ne)^2} \left[\frac{2 \sigma (a + 2ne)}{(b + e)a} - \frac{\rho g_c}{g_c} L \sin \theta \right]$
Annuli		$\frac{C \dot{m} \mu L}{2 \rho \pi (r_o - r_i)^4 g_c}$	$\frac{2 \sigma}{r_o - r_i}$	$\frac{\rho \lambda g_c b^3}{12 \mu L} \left[\frac{2 \sigma}{b} - \frac{\rho g_c}{g_c} L \sin \theta \right], b = r_o - r_i$
Rectangular Channels		$\frac{2C \dot{m} \mu L (a + b)^2}{\rho 4(ab)^3 g_c}$	$\frac{2(a + b)}{ab} \sigma$	Square $a = b, C = 14.23$ $\frac{\rho \lambda g_c a^3}{28.6 \mu L} \left[\frac{4 \sigma}{a} - \frac{\rho g_c}{g_c} L \sin \theta \right]$
Rectangular Channels		$\frac{3 \dot{m} \mu L (2b + a)^2}{\rho (ab)^3 g_c}$	$\frac{(2b + a)}{ab} \sigma$	$\frac{\rho \lambda a^2 b^3 g_c}{3 \mu L (2b + a)^2} \left[\frac{(2b + a) \sigma}{ab} - \frac{\rho g_c}{g_c} L \sin \theta \right]$
V Grooves		$\frac{8C \dot{m} \mu L \tan \frac{\alpha}{2} \left[\tan \frac{\alpha}{2} + \sec \frac{\alpha}{2} \right]^2}{\rho A^4 g_c}$	$\frac{4 \sigma (\tan \frac{\alpha}{2} + \sec \frac{\alpha}{2})}{A}$	60° (Equilateral Triangle), $C = 13.33$ $\frac{\rho \lambda g_c A^3}{106.64 \mu L \tan \frac{\alpha}{2}} \left[\frac{4 \sigma (\tan \frac{\alpha}{2} + \sec \frac{\alpha}{2})}{A} - \frac{\rho g_c}{g_c} L \sin \theta \right]$
V Grooves		$\frac{112 \dot{m} \mu L \sin \frac{\alpha}{2}}{\rho A^4 (\cos \frac{\alpha}{2})^2 g_c}$	$\frac{4 \sec \frac{\alpha}{2} \sigma}{A}$	$\frac{\rho \lambda A^3 (\cos^2 \frac{\alpha}{2}) g_c}{112 \mu L (\sin \frac{\alpha}{2})} \left[\frac{4 (\sec \frac{\alpha}{2}) \sigma}{A} - \frac{\rho g_c}{g_c} L \sin \theta \right]$
Pleated Screens		$\frac{C \dot{m} \mu L (w + \pi r)^2}{16 r^3 \rho (w + 2r)^3 g_c}$	$\frac{(\pi r + w) \sigma}{r(w + 2r)}$	$\frac{4 r^2 (w + 2r)^3 \rho \lambda g_c}{C (w + \pi r)^2 \mu L} \left[\frac{(\pi r + w) \sigma}{r(w + 2r)} - \frac{\rho g_c}{g_c} L \sin \theta \right]$
Pleated Screens		$\frac{C \dot{m} \mu L (w + (\pi + 2)r)^2}{16 r^3 \rho (w + 2r)^3 g_c}$	$\frac{(w + (\pi + 2)r) \sigma}{r(w + 2r)}$	$\frac{4 r^2 (w + 2r)^3 \rho \lambda g_c}{C [w + (\pi + 2)r]^2 \mu L} \left[\frac{(w + (\pi + 2)r) \sigma}{r(w + 2r)} - \frac{\rho g_c}{g_c} L \sin \theta \right]$
Screen		$\frac{V_W A_F \mu L}{K_1 A_T g_c}$ A_F = flow area A_T = total cross sectional area K_1 = permeability B = an empirical constant	$\frac{\phi \sigma}{D_s}$	$\frac{\rho \lambda g_c}{\mu L} B p t \left[\sigma - \frac{\rho g_c}{g_c} \frac{D_s}{\phi} L \sin \theta \right]$

Table 2 Selected specimen geometries^a

Plate/screen-screen/plate, specimen 1	$b = 0.035$ in.
Plate/screen-screen/plate, specimen 2	$b = 0.044$ in.
Plate/screen-screen/plate, specimen 3	$b = 0.056$ in.
Screen/plate-plate/screen, specimen 1	$b = 0.020$ in.
Screen/plate-plate/screen, specimen 2	$b = 0.025$ in.
Screen/plate-plate/screen, specimen 3	$b = 0.038$ in.
Pleated screen, specimen 1 ^b	$t = 0.15$ in.
	$p = 0.088$ in.
	$N = 4$
Plate/screen-plate/screen, specimen 1	$b = 0.025$ in.
Plate/screen-plate/screen, specimen 2	$b = 0.044$ in.

^a Where b is distance between inner barriers, p is pleat pitch (distance between corresponding points on adjacent pleats), t is the pleat depth, and N is screen surface area divided by projected area.

^b Minimum pleat pitch and depth for 18-in.-long pleat.

Fixtures were fabricated for clamping and holding the reference screen specimens during testing. Three coplanar knife edges supported the more rigid sandwich configurations and pleated screen. For some tests, the reservoir edge replaced the knife edge nearest the reservoir to minimize dripping from the specimens.

Two levelers, consisting of plastic troughs filled with test fluid, were mounted at right angles to each other on the baseplate. These were used in conjunction with a tooling transit to control specimen orientation. With this arrangement, the end of the specimen, approximately 17 in. from the source, could be positioned vertically within 0.001 in.

To supply liquid (ethanol) to the test specimen, the upstream side of the specimen was bent down below the edge of the reservoir. The reservoir was kept full to the top of the wick by adjusting a needle valve on the reservoir refill. A fast drain was also provided for initially filling the reservoir or draining the reservoir refill.

Evaporation of liquid within the test enclosure was minimized by maintaining GN₂ saturated with ethanol in the experiment enclosure. This was accomplished with a pressurized humidifier, containing a 26-W aquarium heater, partially filled with test fluid through which gaseous nitrogen (boiled off from liquid nitrogen) was bubbled. An aquarium

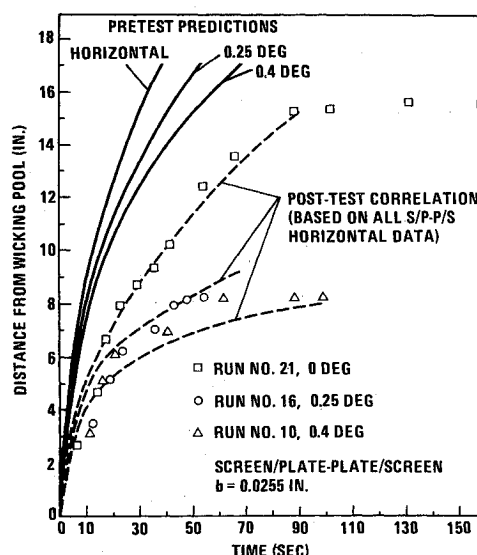


Fig. 3 Predicted and actual wicking for 50 × 250-mesh screen/plate-plate/screen configurations.

air stone was used to disperse the GN₂ bubbles and the heater was used to replace the heat lost in vaporizing the test fluid. The humidifier was kept several degrees below the test enclosure temperature to prevent liquid condensation on the enclosure surfaces and possible degradation in viewing the wicking. A qualitative humidity indicator made of screen was wetted before each run and examined periodically to note any drying due to ethanol evaporation.

The test enclosure was vented out of the environmentally controlled room to reduce fire potential and to protect test personnel from respiratory hazards. A timer, mounted in the field of view of the camera, was used to measure wicking time. Rulers aligned on the side of wicking specimens measured the distance traveled by the wicking fluid. Thermocouples on the apparatus and reference test specimen measured the absolute temperature of the enclosure and specimens and the differential between the humidifier and the enclosure. Checkout of the apparatus with the reference

Fig. 2 Experiment apparatus.

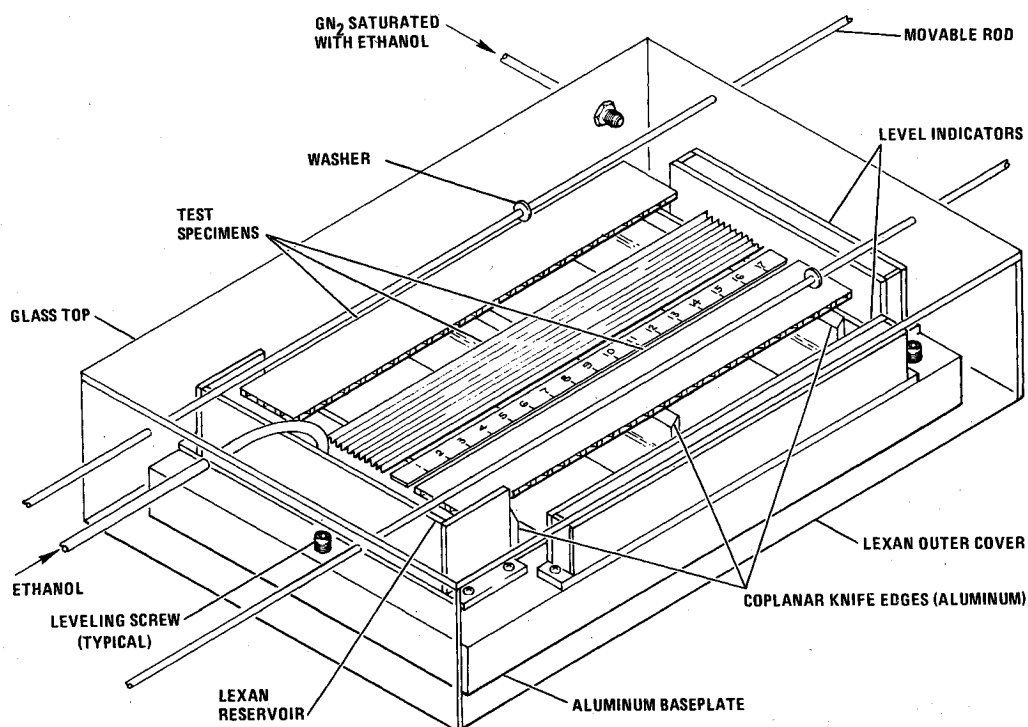


Table 3 Wicking correction factors

Configuration	Screen	Spacing, in.	ΔP_o , psf	ΔP_x , psf	$\Delta P_{x, \text{mean}}$, psf
Plate/screen-screen/plate	200 × 1400	0.0445	0.825	0.384	} 0.397
		0.056	0.656	0.41	
Plate/screen-screen/plate	50 × 250	0.034	1.08	0.329	} 0.393
		0.0445	0.825	0.44	
		0.056	0.656	0.42	
Screen/plate-plate/screen	50 × 250	0.02	0.914	0.509	} 0.551
		0.0255	0.811	0.56	
		0.034	0.69	0.55	
		0.034	0.69	0.56	
		0.034	0.69	0.585	
Plate/screen-plate/screen	50 × 250	0.0255	0.53	0.11	} 0.183
		0.034	0.43	0.258	
		0.0445	0.35	0.181	
Pleated screen	50 × 250	$p = 0.088$ $t = 0.15$	0.97	0.34	0.34

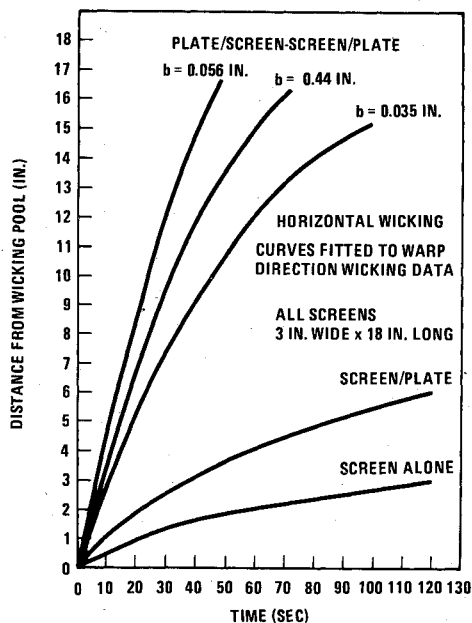


Fig. 4 Increased wicking capability for plate/screen-screen/plate and screen/plate configurations.

specimens showed that temperature differences along the wicking front were negligible. Consequently, thermocouples were not attached to the other wicking test specimens. The humidifier heater was controlled according to the temperature differential between the humidifier and enclosure.

Originally, it was thought that screen wetting would be instantaneous and the wicking front could be recorded by photographing the wetting of the top screen. This proved to be an inaccurate method of recording the position of the wicking front inside the specimen since, in many cases, the top screen wicked ahead of the liquid inside the wick. An indirect method was therefore used to photograph the wicking front. The washers, shown in Fig. 2, were aligned with the wicking front by sliding a metal rod along as the fluid wicking progressed. With this observation method, only the two end specimens could be recorded simultaneously unless the middle specimen was the pleated screen. The pleated screen wicking

was photographed directly. Testing was conducted using 200-proof reagent grade ethanol with specimens at 0, 0.1, 0.25, or 0.4 deg to the horizontal. A total of 36 runs were made.

Data Correlation

Wicking distance versus time was determined by careful inspection of the film results. Linear regression analysis of several runs indicated that the effect of evaporation on test results was negligible. A correction factor was made to account for screen filling, and data were fitted to several possible correlating equations. The equation that best fit the horizontal data was one of the form

$$\Delta P_o = \Delta P_f + \Delta P_x \quad (7)$$

Equation (7) was evaluated using measured geometry to compute ΔP_o and measured values of L and Δt , over the entire range of L and Δt . Figure 3 shows the predicted values of wicking distance vs time for a typical wicking configuration. The post-test correlation curves are also shown, indicating the reduction in wicking that was experienced. Several additional correlation curves are presented in Ref. 3.

Figure 4 shows the improvement in horizontal wicking obtained using plate/screen-screen/plate wicks compared to screen/plate and to screen alone. Screen/plate gives better wicking than screen alone, because the screen was spotwelded to the plate on only a few dozen lands on the perforated plate. This leaves a path between the screen and plate where they are not in intimate contact.

Values of ΔP_x obtained for each configuration are given in Table 3. Note that close agreement between the ΔP_x terms found for the 50 × 250 and 200 × 1400 screens. Equation (6) can be used as a design tool for heat interception capability using the wicking correction factors in Table 3 and the empirical relationship expressed in Eq. (7). The driving pressure ΔP_o , in Eq. (6) is reduced directly by the correction term ΔP_x . Calculations of minimum, maximum, and optimum spacing can be determined by applying Eq. (6) to anticipated capillary device heat flux, wicking length, and acceleration conditions.

Wicking capability and wick spacing are functions of the gravity dependence of ΔP_x . Using worst-case interpretations, plate/screen-screen/plate and plate/screen-plate/screen configurations were sized for LO₂ and LH₂ start baskets. Total weight of the passively cooled baskets was found to be 198.6 lb_m—a hardware weight savings to 129 lb_m over an actively cooled system. In addition, a payload penalty of 418

lb_m results from dumping vent fluid overboard for actively cooled capillary devices in the five-burn mission.

Conclusions

Passive cooling appears to be a promising method of thermal conditioning cryogenic capillary acquisition devices. Plate/screen-screen/plate and plate/screen-plate/screen are the two most attractive capillary pumping candidates for the Centaur D-1S. These configurations offer a payload advantage for the five-burn mission over actively cooled systems that dump fluid directly overboard. Their completely passive operation provides reduced complexity and increased reliability.

References

- ¹Blatt, M. H. and Aydelott, J. C., "Centaur Propellant Acquisition System," *Journal of Spacecraft and Rockets*, Vol. 13, Sept. 1976, pp. 515-521.
- ²Bock, E. H., et al., "Centaur/Shuttle Integration Study," General Dynamics Convair Division Rept. GDCA-BNZ 73-006-8, NAS3-16786, NASA CR-134488, Dec. 1973.
- ³Blatt, M. H., Pleasant, R. L., and Erickson, R. C., "Centaur Propellant Thermal Conditioning System," General Dynamics Convair Division Rept. CASD-NAS-76-026, NAS-19693, NASA CR135032, July 1976.
- ⁴Bressler, R. G. and Wyatt, P. W., "Surface Wetting Through Capillary Grooves," *Transactions of the ASME, Journal of Heat Transfer*, Vol. 92, Feb. 1970, pp. 126-132.

From the AIAA Progress in Astronautics and Aeronautics Series . . .

THERMOPHYSICS OF SPACECRAFT AND OUTER PLANET ENTRY PROBES—v. 56

Edited by Allie M. Smith, ARO Inc., Arnold Air Force Station, Tennessee

Stimulated by the ever-advancing challenge of space technology in the past 20 years, the science of thermophysics has grown dramatically in content and technical sophistication. The practical goals are to solve problems of heat transfer and temperature control, but the reach of the field is well beyond the conventional subject of heat transfer. As the name implies, the advances in the subject have demanded detailed studies of the underlying physics, including such topics as the processes of radiation, reflection and absorption, the radiation transfer with material, contact phenomena affecting thermal resistance, energy exchange, deep cryogenic temperature, and so forth. This volume is intended to bring the most recent progress in these fields to the attention of the physical scientist as well as to the heat-transfer engineer.

467 pp., 6 × 9, \$20.00 Mem. \$40.00 List

TO ORDER WRITE: Publications Dept., AIAA, 1290 Avenue of the Americas, New York, N. Y. 10019